Energy Engineering

Tech Science Press

Doi:10.32604/ee.2025.074766

ARTICLE

Small-Signal Stability Analysis of Solar-Storage Hybrid Heterogeneous Power Generation Systems Based on Graphical Block-Oriented Modeling

Qiang Liu[1], Yongqiang Zhou[1], Chaoyang Lu[2], Zhen Yan[1], Yanwen Li[1], Gangui Yan[2] and Yupeng Wang[2,*]

[1]Xingtai Power Supply Branch, State Grid Hebei Electric Power Co., Ltd., Xingtai, 054001, China

[2]Key Laboratory of Modern Power System Simulation and Control & Renewable Energy Technology, Ministry of Education (Northeast Electric Power University), Jilin, 132012, China

*Corresponding Author: Yupeng Wang. Email: 20172753@neepu.edu.cn

Received: 17 October 2025; Accepted: 16 December 2025; Published: 18 October 2026

ABSTRACT: Hybrid photovoltaic and energy storage systems play a critical role in enhancing grid stability; however, the sub-synchronous oscillation issues induced by their power electronic interfaces cannot be overlooked. This study proposes a graphical block-based modeling method for a hybrid power generation system composed of grid-following (GFL) photovoltaic and grid-forming (GFM) energy storage units. The method abstracts each system component into graphical modules with clearly defined interfaces, enables intuitive construction in the Matlab/Simulink environment, and utilizes built-in functions to automatically generate global system equations. While ensuring model accuracy, it significantly improves modeling intuitiveness, efficiency, and scalability, and avoids algebraic errors that are difficult to eliminate in traditional manual derivations. Based on the constructed model, this paper identifies the dominant sub-synchronous oscillation modes of the system through eigenvalue analysis. Furthermore, using the root locus method, it systematically reveals the dynamic influence of key control parameters of the GFM energy storage unit—such as the active voltage proportional coefficient $k_{p1,M}$, the reactive voltage proportional coefficient $k_{p2,M}$, the reactive voltage integral coefficient $k_{i2,M}$, and the reactive current integral coefficient $k_{i4,M}$—on the small-signal stability of the system. The research shows that reasonably increasing these key parameters can effectively enhance the small-signal stability of the photovoltaic-storage hybrid system. Finally, time-domain simulation results verify the correctness of the proposed modeling method and related conclusions, thereby providing a theoretical basis for the stable operation and controller design of hybrid photovoltaic-storage power generation systems.

KEYWORDS: GFL photovoltaic; GFM energy storage; solar-storage hybrid power generation system; state-space model; graphical block-based modeling; small-signal stability analysis

1 Introduction

The increased use of photovoltaic power generation in power systems has meant that solar-storage hybrid power generation systems have become one of the key solutions for mitigating photovoltaic power fluctuations and enhancing grid operational flexibility [1,2]. Combining energy storage units (such as battery energy storage) with photovoltaic generation effectively alleviates the impacts of intermittent and stochastic photovoltaic outputs on the grid and allows the system to participate in ancillary services, such as frequency and voltage regulation, thereby improving the grid capacity to absorb renewable energy. However, solar-storage systems generally rely on power electronic converters for energy conversion and control [3]. Their high penetration enhances system controllability but they also introduce stability challenges, particularly

Copyright © 2026 The Authors. Published by Tech Science Press.
This work is licensed under a Creative Commons Attribution 4.0 International License, which permits unrestricted use, distribution, and reproduction in any medium, provided the original work is properly cited.

the frequent occurrence of wide-band oscillations, which have become a significant threat to the secure and stable operation of power systems.

Solar-storage hybrid power generation systems are highly dependent on power electronic converters and the control strategies used by these converters determine the dynamic characteristics of a system [4,5]. Previous studies on photovoltaic generation units typically adopted grid-following (GFL) control to maximize utilization of the photovoltaic generation potential [6]; however, energy storage systems are progressively using grid-forming (GFM) control strategies to enhance active grid support capabilities [7]. The significant differences in dynamic characteristics between these two control strategies may lead to complex interactive oscillation issues in hybrid configurations. Among these, sub-synchronous oscillation has become a major factor affecting small-signal stability due to its wide frequency band and complex mechanism [8–10].

Current research on modeling hybrid power generation systems containing grid-following and grid-forming converters primarily revolves around two methodologies: impedance analysis and state-space analysis. In terms of frequency-domain impedance modeling, Reference [11] establishes a single-input single-output model for solar-storage hybrid power generation systems, constructing a corresponding dynamic interaction model to analyze the impact of different control loops and parameters on system small-signal stability. However, the accuracy and applicability of this method in scenarios requiring precise quantitative analysis, particularly when strong coupling effects exist within the system, remain questionable. Reference [12] develops a system impedance model, identifying the filter inductance of grid-forming converters as a critical parameter affecting stability under weak grid conditions. The study finds that system stability margins are lowest at maximum photovoltaic output and proposes an integrated parameter design strategy for grid-forming converters oriented toward stability. Reference [13] employs incremental impedance and state-space models to reveal the mechanism by which hybrid power generation systems trigger low-frequency oscillation instability when photovoltaics operate in the current-limiting region under weak grid conditions. Furthermore, it proposes a novel active damping strategy based on reshaping DC-link dynamics, which effectively resets unstable modes and enhances system stability. Although the models constructed in these frequency-domain impedance studies exhibit strong scalability, their inherent "port-based" and "black-box" characteristics make it difficult to directly observe the dynamic processes of internal state variables. Additionally, in complex systems involving multiple converters, such methods struggle to accurately identify dominant instability paths, limiting their in-depth application in engineering practice.

In the domain of state-space modeling, Reference [14] establishes a detailed state-space model, clearly revealing that the dynamic interaction between power loops and current loops is a key factor influencing small-disturbance stability when grid-forming and grid-following converters operate in parallel. However, this analysis is primarily based on simplified models, resulting in insufficient precision in quantifying interaction strength and weak model scalability. Reference [15] applies the state-space method to develop a refined model for the control interactions between offshore wind power and grid-forming energy storage systems. Nevertheless, the model exhibits high complexity, substantial computational demands, and limited physical intuitiveness, making it difficult to quickly identify dominant oscillation modes and key influencing factors. Reference [16] further constructs a full-order state-space model for a hybrid photovoltaic-wind-storage system, simplifying it into a reduced-order model based on participation factor analysis to study system dynamic interactions and stability. However, the overall process remains relatively complex and computationally burdensome. In general, while state-space model-based analysis methods offer advantages in theoretical rigor and result accuracy, they commonly suffer from high computational load, solution complexity, and poor scalability, particularly when applied to large-scale complex systems.

Based on this literature analysis, the novel contributions made by this study are as follows:

(1) A full-order state-space model of a hybrid solar-storage power generation system has been established along with an efficient graphical block-based modeling method. Full-order state-space equations for a hybrid power generation system containing GFL photovoltaic units and GFM energy storage units were derived and a graphical block-based modeling method based on these equations is proposed that abstracts each component in the system into graphical modules with clearly defined input-output interface relationships. The model was visually constructed in the Matlab/Simulink environment and global system equations were automatically generated using its built-in functions. This method avoids algebraic errors that are difficult to eliminate in traditional manual derivations and eliminates the need for cumbersome intermediate variable elimination processes. Consequently, it significantly improves modeling efficiency and scalability while ensuring model accuracy.

(2) The graphical block-based model was used to identify the dominant system oscillation modes and the dynamic influence patterns for key parameters have been identified. Building upon the constructed graphical block-based model, this study used an eigenvalue analysis to accurately identify the modes that can induce subsynchronous oscillations in the system. In addition, a root locus analysis was used to systematically investigate the dynamic patterns of the key GFM energy storage unit control parameters that influenced the dominant eigenvalues in the complex plane. This analysis revealed the intrinsic relationship between the control parameters and the small-signal stability margin of the system, clarified the influence patterns of each parameter on the eigenvalues for the dominant subsynchronous oscillation modes in the hybrid solar-storage power generation system, and provides a clear theoretical basis for subsequent optimization of the controller design.

(3) A detailed electromagnetic transient simulation model was constructed to validate the effectiveness of the proposed method and the analytical conclusions. The accuracy of the theoretical analysis was verified by developing detailed simulation models that corresponded to the state-space model on both the Matlab/Simulink and PSCAD/EMTDC platforms. The accuracy of the theoretical analysis was confirmed by setting up multiple typical operating conditions and observing the dynamic response of the system before and after adjusting the key parameters that affect GFM energy storage. The cross-platform validation results consistently demonstrated that the proposed graphical modeling method was accurate and reliable and that the parameter influence laws derived from this model were correct and effective.

2 Small-Signal Modeling of GFL Photovoltaic and GFM Energy Storage Hybrid Power Generation Systems

This study took the GFL photovoltaic and GFM energy storage hybrid power generation system as the research object and a schematic diagram of the system structure is shown in Fig. 1. Subscript L is used to denote GFL photovoltaic parameters, subscript M denotes the GFM energy storage parameters, and subscript 0 denotes the initial variable values. There were two different d/q coordinate systems: the coordinate system formed by d/q transformation using the phase generated by the synchronization control loop and phase-locked loop is defined as the control d/q coordinate system and the coordinate system formed by the actual main circuit d/q transformation is defined as the main circuit d/q coordinate system. A coordinate transformation was used to convert the small-signal state equations in the control d/q coordinate system to the main circuit d/q coordinate system, thereby establishing a small-signal model of the GFL photovoltaic and GFM energy storage hybrid power generation system in the main circuit coordinate system.

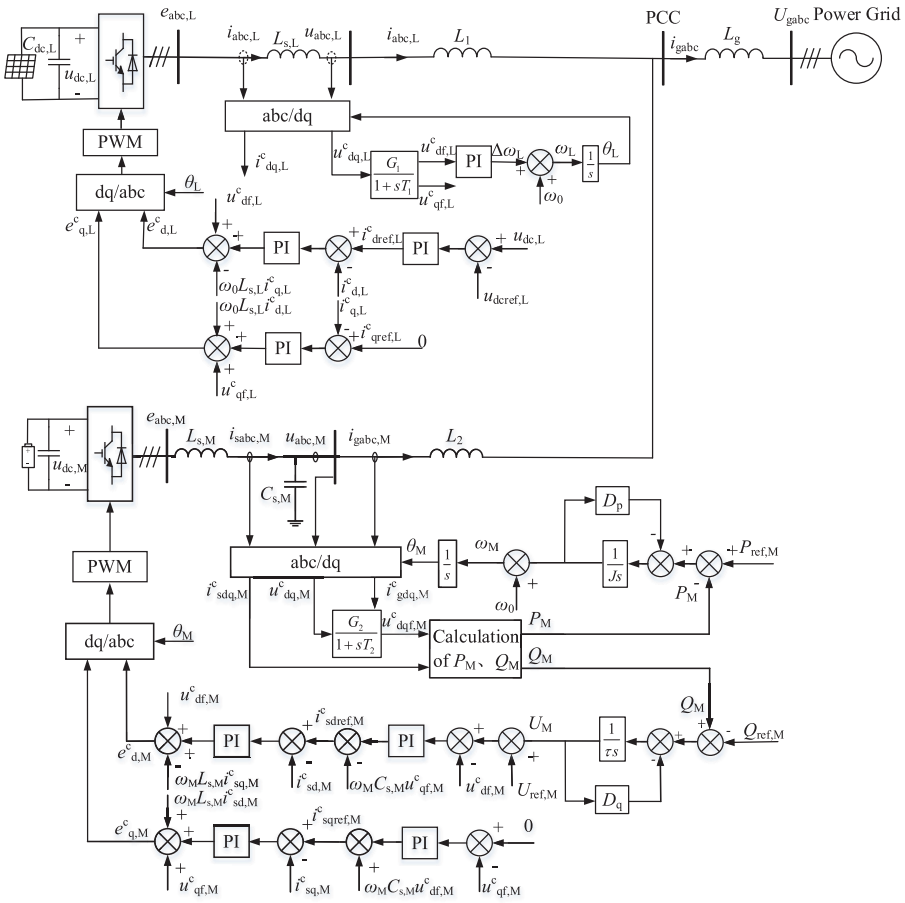


Figure 1: Grid-forming energy storage grid connected system model

2.1 GFL Photovoltaic Small-Signal Model

To simplify the analysis, the DC-side input by the GFL photovoltaic system was assumed to be equivalent to a controlled current source. Additionally, stator voltage vector control was adopted with the stator voltage oriented along the *d*-axis. These assumptions meant that the initial components of the *q*-axis voltage and current were zero. Linearizing at the operating point produced a small-signal model of the DC capacitor as follows:

$$\begin{cases} C_{\mathrm{dc,L}} u_{\mathrm{dc,L0}} \dfrac{\mathrm{d}\Delta u_{\mathrm{dc,L}}}{\mathrm{d}t} = \Delta P_{\mathrm{in,L}} - \Delta P_{\mathrm{out,L}} \\ \Delta P_{\mathrm{in,L}} = I_{\mathrm{dc,L0}} \Delta u_{\mathrm{dc,L}} \\ \Delta P_{\mathrm{out,L}} = 1.5 u_{\mathrm{d,L0}} \Delta i_{\mathrm{d,L}} + 1.5 i_{\mathrm{d,L0}} \Delta u_{\mathrm{d,L}} \end{cases} \tag{1}$$

where $C_{\mathrm{dc,L}}$ is the DC-side capacitor of the GFL photovoltaic system; $u_{\mathrm{dc,L0}}$, $u_{\mathrm{d,L0}}$, and $i_{\mathrm{d,L0}}$ are the steady-state values of the DC-side capacitor voltage, *d*-axis output voltage, and *d*-axis output current of the GFL photovoltaic system, respectively; $I_{\mathrm{dc,L0}}$ is the steady-state output current of the controlled current source in the GFL photovoltaic system; $\Delta u_{\mathrm{dc,L}}$ is the small-signal disturbance component of the DC-side capacitor voltage of the GFL photovoltaic system; ΔP_{in} and ΔP_{out} are the small-signal disturbance components of the input power and output power of the GFL photovoltaic system, respectively; $\Delta i_{\mathrm{d,L}}$ and $\Delta u_{\mathrm{d,L}}$ are the small-signal disturbance components of the *d*-axis output current and *d*-axis output voltage of the GFL photovoltaic system, respectively.

The small-signal model of the GFL photovoltaic filter inductor component is as follows:

$$\begin{cases} L_{s,L}\dfrac{d\Delta i_{d,L}}{dt} = \Delta e_{d,L} - \Delta u_{d,L} + \omega_0 L_{s,L}\Delta i_{q,L} \\ L_{s,L}\dfrac{d\Delta i_{q,L}}{dt} = \Delta e_{q,L} - \Delta u_{q,L} - \omega_0 L_{s,L}\Delta i_{d,L} \end{cases} \tag{2}$$

where $L_{s,L}$ is the filter inductor of the GFL photovoltaic inverter; $\Delta e_{d,L}$ and $\Delta e_{q,L}$ are the small-signal disturbance components of the d/q-axis converter terminal voltage of the GFL photovoltaic system, respectively; $\Delta u_{d,L}$ and $\Delta u_{q,L}$ are the small-signal disturbance components of the d/q-axis output voltage of the GFL photovoltaic system, respectively; $\Delta i_{d,L}$ and $\Delta i_{q,L}$ are the small-signal disturbance components of the d/q-axis output current of the GFL photovoltaic system, respectively; and ω_0 is the rated angular frequency.

The obtained d/q-axis voltages $u_{d,L}$ and $u_{q,L}$ at the point of common coupling (PCC) of the GFL photovoltaic system were filtered and linearized at the operating point. The small-signal model in the main circuit d/q coordinate system is as follows:

$$\begin{cases} \dfrac{d\Delta u_{df,L}}{dt} = \dfrac{G_1}{T_1}\Delta u_{d,L} - \dfrac{1}{T_1}\Delta u_{df,L} \\ \dfrac{d\Delta u_{qf,L}}{dt} = \dfrac{G_1}{T_1}\Delta u_{q,L} - \dfrac{1}{T_1}\Delta u_{qf,L} \end{cases} \tag{3}$$

where $\Delta u_{df,L}$ and $\Delta u_{qf,L}$ are the small-signal disturbance components of the filtered d/q-axis output voltages of the GFL photovoltaic system, respectively; G_1 and T_1 are the steady-state gain and time constant of the GFL photovoltaic filter, respectively.

The filtered d/q-axis voltages $u_{df,L}$ and $u_{qf,L}$ were used to control the GFL photovoltaic system. Consequently, the small-signal model of the phase-locked loop in the main circuit d/q coordinate system can be derived as follows:

$$\begin{cases} \dfrac{d\Delta x_{1,L}}{dt} = \Delta u_{qf,L} - u_{df,L0}\Delta\theta_L \\ \dfrac{d\Delta\theta_L}{dt} = k_{p1,L}\left(\Delta u_{qf,L} - u_{df,L0}\Delta\theta_L\right) + k_{i1,L}\Delta x_{1,L} \end{cases} \tag{4}$$

where $\Delta x_{1,L}$ is the small-signal disturbance component of the intermediate state variable of the GFL photovoltaic phase-locked loop; $\Delta u_{df,L0}$ is the steady-state value of the filtered d-axis output voltage of the GFL photovoltaic system; $k_{p1,L}$ and $k_{i1,L}$ are the proportional and integral coefficients of the GFL photovoltaic phase-locked loop, respectively; and $\Delta\theta_L$ is the small-signal disturbance component of the output angle of the GFL photovoltaic phase-locked loop.

The small-signal model of the active voltage outer loop in the main circuit d/q coordinate system for GFL photovoltaic control is as follows:

$$\frac{d\Delta x_{2,L}}{dt} = \Delta u_{dc,L} \tag{5}$$

where $\Delta x_{2,L}$ is the small-signal disturbance component of the intermediate state variable in the active power-voltage outer loop of the GFL photovoltaic system, and $\Delta u_{dc,L}$ is the small-signal disturbance component of the DC-side capacitor voltage of the GFL photovoltaic system.

The small-signal model of the current inner loop control for GFL photovoltaic systems in the main circuit d/q coordinate frame is expressed as follows:

$$\begin{cases} \dfrac{\mathrm{d}\Delta x_{3,\mathrm{L}}}{\mathrm{d}t} = k_{\mathrm{p2,L}}\Delta u_{\mathrm{dc,L}} + k_{\mathrm{i2,L}}\Delta x_{2,\mathrm{L}} - \Delta i_{\mathrm{d,L}} \\ \dfrac{\mathrm{d}\Delta x_{4,\mathrm{L}}}{\mathrm{d}t} = -\Delta i_{\mathrm{q,L}} + i_{\mathrm{d,L0}}\Delta\theta_{\mathrm{L}} \end{cases} \tag{6}$$

where $\Delta x_{3,\mathrm{L}}$ is the small-signal disturbance component of the intermediate state variable in the active current inner loop of the GFL photovoltaic system; $\Delta x_{4,\mathrm{L}}$ is the small-signal disturbance component of the intermediate state variable in the reactive current inner loop of the GFL photovoltaic system; $\Delta i_{\mathrm{d,L}}$ and $\Delta i_{\mathrm{q,L}}$ are the small-signal disturbance components of the d/q-axis output currents of the GFL photovoltaic system, respectively; $k_{\mathrm{p2,L}}$ and $k_{\mathrm{i2,L}}$ are the proportional and integral coefficients of the GFL photovoltaic active power-voltage outer loop, respectively; and $i_{\mathrm{d,L0}}$ is the steady-state value of the d-axis output current of the GFL photovoltaic system.

2.2 GFM Energy Storage Small-Signal Model

The isolation effect of the DC-AC converter in the GFM energy storage system and the presence of substantial support capacitance on the DC side meant that the DC-DC module was equivalent to an ideal DC voltage source. Therefore, the dynamic process on the DC side was not considered when establishing the small-signal model of grid-forming energy storage.

The LC filter model for GFM energy storage is as follows:

$$\begin{cases} L_{\mathrm{s,M}}\dfrac{\mathrm{d}\Delta i_{\mathrm{sd,M}}}{\mathrm{d}t} = \Delta e_{\mathrm{d,M}} - \Delta u_{\mathrm{d,M}} + \omega_0 L_{\mathrm{s,M}}\Delta i_{\mathrm{sq,M}} \\ L_{\mathrm{s,M}}\dfrac{\mathrm{d}\Delta i_{\mathrm{sq,M}}}{\mathrm{d}t} = \Delta e_{\mathrm{q,M}} - \Delta u_{\mathrm{q,M}} - \omega_0 L_{\mathrm{s,M}}\Delta i_{\mathrm{sd,M}} \end{cases}, \begin{cases} C_{\mathrm{s,M}}\dfrac{\mathrm{d}\Delta u_{\mathrm{d,M}}}{\mathrm{d}t} = \Delta i_{\mathrm{sd,M}} - \Delta i_{\mathrm{gd,M}} + \omega_0 C_{\mathrm{s,M}}\Delta u_{\mathrm{q,M}} \\ C_{\mathrm{s,M}}\dfrac{\mathrm{d}\Delta u_{\mathrm{q,M}}}{\mathrm{d}t} = \Delta i_{\mathrm{sq,M}} - \Delta i_{\mathrm{gq,M}} - \omega_0 C_{\mathrm{s,M}}\Delta u_{\mathrm{d,M}} \end{cases} \tag{7}$$

where $L_{\mathrm{s,M}}$ and $C_{\mathrm{s,M}}$ are the filter inductor and filter capacitor of the GFM energy storage system, respectively; $\Delta i_{\mathrm{sd,M}}$ and $\Delta i_{\mathrm{sq,M}}$ are the small-signal disturbance components of the d/q-axis converter output currents of the GFM energy storage system, respectively; $\Delta e_{\mathrm{d,M}}$ and $\Delta e_{\mathrm{q,M}}$ are the small-signal disturbance components of the d/q-axis converter output voltages of the GFM energy storage system, respectively; $\Delta u_{\mathrm{d,M}}$ and $\Delta u_{\mathrm{q,M}}$ are the small-signal disturbance components of the d/q-axis LC filter capacitor voltages of the GFM energy storage system, respectively; $\Delta i_{\mathrm{gd,M}}$ and $\Delta i_{\mathrm{gq,M}}$ are the small-signal disturbance components of the d/q-axis output currents after LC filtering in the GFM energy storage system, respectively; and ω_0 is the rated angular frequency.

The obtained d/q-axis voltages $u_{\mathrm{d,M}}$ and $u_{\mathrm{q,M}}$ at the PCC were filtered and linearized at the operating point. The small-signal model for the main circuit d/q coordinate system is expressed as follows:

$$\begin{cases} \dfrac{\mathrm{d}\Delta u_{\mathrm{df,M}}}{\mathrm{d}t} = \dfrac{G_2}{T_2}\Delta u_{\mathrm{d,M}} - \dfrac{1}{T_2}\Delta u_{\mathrm{df,M}} \\ \dfrac{\mathrm{d}\Delta u_{\mathrm{qf,M}}}{\mathrm{d}t} = \dfrac{G_2}{T_2}\Delta u_{\mathrm{q,M}} - \dfrac{1}{T_2}\Delta u_{\mathrm{qf,M}} \end{cases} \tag{8}$$

where $\Delta u_{\mathrm{df,M}}$ and $\Delta u_{\mathrm{qf,M}}$ are the small-signal disturbance components on the d/q-axis of the LC filter capacitor voltage in the GFM energy storage system after filtering, respectively; G_2 and T_2 are the steady-state gain and time constant of the GFM energy storage filter, respectively.

The synchronization module for GFM energy storage was divided into the active power-frequency and its reactive power-voltage components. The small-signal model for the GFM energy storage synchronization module is as follows:

$$\begin{cases} J\dfrac{\mathrm{d}\Delta\omega_{\mathrm{M}}}{\mathrm{d}t} = -\Delta P_{\mathrm{M}} - D_{\mathrm{p}}\Delta\omega_{\mathrm{M}} \\ \tau\dfrac{\mathrm{d}\Delta U_{\mathrm{M}}}{\mathrm{d}t} = -\Delta Q_{\mathrm{M}} - D_{\mathrm{q}}\Delta U_{\mathrm{M}} \\ \dfrac{\mathrm{d}\Delta\theta_{\mathrm{M}}}{\mathrm{d}t} = \Delta\omega_{\mathrm{M}} \end{cases} \tag{9}$$

where J and D_{p} are the virtual active inertia and virtual active damping of the GFM energy storage system, respectively; τ and D_{q} are the virtual reactive inertia and virtual reactive damping of the GFM energy storage system, respectively; ΔP_{M} and ΔQ_{M} are the small-signal disturbance components of the active output power and reactive output power of the GFM energy storage system, respectively; $\Delta\omega_{\mathrm{M}}$ is the small-signal disturbance component of the angular velocity generated by the active power synchronization loop of the GFM energy storage system; ΔU_{M} is the small-signal disturbance component of the d-axis voltage reference generated by the reactive power synchronization loop of the GFM energy storage system; and $\Delta\theta_{\mathrm{M}}$ is the small-signal disturbance component of the angle generated by the active power synchronization loop of the GFM energy storage system.

Where ΔP_{M} and ΔQ_{M} are given by

$$\begin{cases} \Delta P_{\mathrm{M}} = 1.5\left(u_{\mathrm{df,M,0}}\Delta i_{\mathrm{sd,M}} + i_{\mathrm{sd,M0}}\Delta u_{\mathrm{df,M}} + i_{\mathrm{sq,M0}}\Delta u_{\mathrm{qf,M}}\right) \\ \Delta Q_{\mathrm{M}} = 1.5\left(i_{\mathrm{sd,M0}}\Delta u_{\mathrm{qf,M}} - u_{\mathrm{df,M0}}\Delta i_{\mathrm{sq,M}} - i_{\mathrm{sq,M0}}\Delta u_{\mathrm{df,M}}\right) \end{cases} \tag{10}$$

where $u_{\mathrm{df,M0}}$ is the steady-state value on the d-axis of the LC filter capacitor voltage in the grid-forming energy storage system after filtering; $i_{\mathrm{sd,M0}}$ and $i_{\mathrm{sq,M0}}$ are the steady-state values of the d/q-axis converter output currents of the GFM energy storage system, respectively.

The GFM energy storage system used dual-loop voltage and current control to ensure the voltage across the LC filter capacitor equaled its reference value. The small-signal model of the GFM energy storage voltage outer loop in the main circuit d/q coordinate system is expressed as follows:

$$\begin{cases} \dfrac{\mathrm{d}\Delta x_{1,\mathrm{M}}}{\mathrm{d}t} = \Delta U_{\mathrm{M}} - \Delta u_{\mathrm{df,M}} \\ \dfrac{\mathrm{d}\Delta x_{2,\mathrm{M}}}{\mathrm{d}t} = -\Delta u_{\mathrm{qf,M}} + u_{\mathrm{df,M0}}\Delta\theta_{\mathrm{M}} \end{cases} \tag{11}$$

where $\Delta x_{1,\mathrm{M}}$ is the small-signal disturbance component of the intermediate state variable in the active power-voltage outer loop of the GFM energy storage system; $\Delta x_{2,\mathrm{M}}$ is the small-signal disturbance component of the intermediate state variable in the reactive power-voltage outer loop of the GFM energy storage system.

The small-signal model of the GFM energy storage current inner loop in the main circuit d/q coordinate system is as follows:

$$\begin{cases} \dfrac{\mathrm{d}\Delta x_{3,\mathrm{M}}}{\mathrm{d}t} = k_{\mathrm{p1,M}}\left(\Delta U_{\mathrm{M}} - \Delta u_{\mathrm{df,M}}\right) + k_{\mathrm{i1,M}}\Delta x_{1,\mathrm{M}} - \omega_0 C_{\mathrm{s,M}}\Delta u_{\mathrm{qf,M}} + \omega_0 C_{\mathrm{s,M}} u_{\mathrm{df,M0}}\Delta\theta_{\mathrm{M}} - \Delta i_{\mathrm{sd,M}} \\ \qquad\qquad -i_{\mathrm{sq,M0}}\Delta\theta_{\mathrm{M}} \\ \dfrac{\mathrm{d}\Delta x_{4,\mathrm{M}}}{\mathrm{d}t} = k_{\mathrm{p2,M}}\left(u_{\mathrm{df,M0}}\Delta\theta_{\mathrm{M}} - \Delta u_{\mathrm{qf,M}}\right) + k_{\mathrm{i2,M}}\Delta x_{2,\mathrm{M}} + \omega_0 C_{\mathrm{s,M}}\Delta u_{\mathrm{df,M}} + C_{\mathrm{s,M}} u_{\mathrm{df,M0}}\Delta\omega_{\mathrm{M}} \\ \qquad\qquad -\Delta i_{\mathrm{sq,M}} + i_{\mathrm{sd,M0}}\Delta\theta_{\mathrm{M}} \end{cases} \tag{12}$$

where $\Delta x_{3,M}$ is the small-signal disturbance component of the intermediate state variable in the active current inner loop of the GFM energy storage system; $\Delta x_{4,M}$ is the small-signal disturbance component of the intermediate state variable in the reactive current inner loop of the GFM energy storage system; $k_{p1,M}$ and $k_{i1,M}$ are the proportional and integral coefficients of the active power-voltage outer loop of the GFM energy storage system, respectively; $k_{p2,M}$ and $k_{i2,M}$ are the proportional and integral coefficients of the reactive power-voltage outer loop of the GFM energy storage system, respectively.

2.3 AC Network Small-Signal Model

The mathematical model of the collector line for the GFL photovoltaic and GFM energy storage hybrid power generation system was linearized at the steady-state operating point, which produced the following small-signal model:

$$\begin{cases} L_1 \dfrac{\mathrm{d}\Delta i_{d,L}}{\mathrm{d}t} = \Delta u_{d,L} - \Delta u_{pccd} + \omega_0 L_1 \Delta i_{q,L} \\ L_1 \dfrac{\mathrm{d}\Delta i_{q,L}}{\mathrm{d}t} = \Delta u_{q,L} - \Delta u_{pccq} - \omega_0 L_1 \Delta i_{d,L} \end{cases}, \begin{cases} L_2 \dfrac{\mathrm{d}\Delta i_{gd,M}}{\mathrm{d}t} = \Delta u_{d,M} - \Delta u_{pccd} + \omega_0 L_2 \Delta i_{gq,M} \\ L_2 \dfrac{\mathrm{d}\Delta i_{gq,M}}{\mathrm{d}t} = \Delta u_{q,M} - \Delta u_{pccq} - \omega_0 L_2 \Delta i_{gd,M} \end{cases}, \tag{13}$$

where L_1 and L_2 are the collector line inductances of the GFL photovoltaic system and the GFM energy storage system, respectively; Δu_{pccd} and Δu_{pccq} are the small-signal disturbance components of the d/q-axis voltages at the PCC, respectively; $\Delta i_{d,L}$ and $\Delta i_{q,L}$ are the small-signal disturbance components of the d/q-axis output current of the GFL photovoltaic system, respectively; $\Delta i_{gd,M}$ and $\Delta i_{gq,M}$ are the small-signal disturbance components of the d/q-axis output currents after LC filtering in the GFM energy storage system, respectively; and ω_0 is the rated angular frequency.

The small-signal model of the AC network for the solar-storage hybrid power generation system is as follows:

$$\begin{cases} L_g \dfrac{\mathrm{d}\left(\Delta i_{d,L} + \Delta i_{gd,M}\right)}{\mathrm{d}t} = \Delta u_{pccd} - \Delta U_{gd} + \omega_0 L_g \left(\Delta i_{q,L} + \Delta i_{gq,M}\right) \\ L_g \dfrac{\mathrm{d}\left(\Delta i_{q,L} + \Delta i_{gq,M}\right)}{\mathrm{d}t} = \Delta u_{pccq} - \Delta U_{gq} - \omega_0 L_g \left(\Delta i_{d,L} + \Delta i_{gd,M}\right) \end{cases} \tag{14}$$

where L_g is the line inductance; ΔU_{gd} and ΔU_{gq} are the small-signal disturbance components of the d/q-axis voltages at the infinite grid, respectively.

The GFL photovoltaic small-signal model established in Section 2.1, the GFM energy storage small-signal model in Section 2.2, and the AC network small-signal model in Section 2.3 were used to construct a full-order state-space model of the GFL photovoltaic and GFM energy storage hybrid power generation system. The state-space equation contained 25 state variables consisting of 10 state variables for the grid-following photovoltaic system and 15 state variables for the grid-forming energy storage system.

The GFL photovoltaic system contained three main state variables (namely $\Delta u_{dc,L}$, $\Delta i_{d,L}$, and $\Delta i_{q,L}$, representing the DC-side capacitor voltage, and the d/q-axis components of the converter output current of the grid-following photovoltaic system) and seven control loop state variables (namely $\Delta x_{1,L}$, $\Delta x_{2,L}$, $\Delta x_{3,L}$, $\Delta x_{4,L}$, $\Delta u_{df,L}$, $\Delta u_{qf,L}$, and $\Delta \theta_L$, representing the indirect state variables of the phase-locked loop, the active power-voltage outer loop, the active current inner loop, and the reactive current inner loop, as well as the d/q-axis components of the filtered output voltage and the angle output by the phase-locked loop).

The GFM energy storage system contained six main state variables (namely $\Delta i_{sd,M}$, $\Delta i_{sq,M}$, $\Delta u_{d,M}$, $\Delta u_{q,M}$, $\Delta i_{gd,M}$, and $\Delta i_{gq,M}$, representing the d/q-axis components of the converter output current, the d/q-axis components of the LC filter capacitor voltage, and the d/q-axis components of the output current after LC filtering) and nine control loop state variables (namely ΔU_M, $\Delta \omega_M$, $\Delta \theta_M$, $\Delta x_{1,M}$, $\Delta x_{2,M}$, $\Delta x_{3,M}$, $\Delta x_{4,M}$, $\Delta u_{df,M}$,

and $\Delta u_{qf,M}$, representing the d-axis voltage reference generated by the reactive power synchronization loop, the angular velocity and the angle generated by the active power synchronization loop; the indirect state variables for the active power-voltage outer loop, the reactive power-voltage outer loop, the active current inner loop, and the reactive current inner loop; and the components of the LC filter capacitor voltage after filtering processing on the d/q-axis).

3 Graphical Block-Oriented Modeling of Solar-Storage Hybrid Power Generation Systems

A derivation process based on the full-order state-space equations for the GFL photovoltaic and GFM energy storage hybrid system derived in the previous section would involve complex mathematical operations and cumbersome elimination of intermediate variables. Therefore, a graphical block-based modeling solution, which abstracts power system components into graphical modules with clear input-output interface relationships, was used. Visual modeling was implemented in Matlab/Simulink and the system state-space equations were automatically generated using the built-in Matlab/Simulink functions. This approach avoided the potential human calculation errors associated the traditional state-space equation derivation and eliminated the need for intermediate algebraic operations to remove intermediate variables. These two improvements significantly improved modeling efficiency.

The specific workflow for the linearized graphical block-based modeling of the GFL photovoltaic and GFM energy storage hybrid power generation system is illustrated in Fig. 2: (1) The GFL photovoltaic system was divided into three independent modules: the DC capacitor, the grid-side control system, and the filter inductor. Simultaneously, the grid-forming energy storage system was divided into three independent modules: the grid-side control system, the filter inductor, and the filter capacitor. Detailed models of each independent module were constructed by formulating equations based on the constraint relationships associated with the respective modules. (2) The independent modules were connected to build the GFL photovoltaic and GFM energy storage unit models based on the GFL photovoltaic unit and the grid-forming energy storage unit structures and the input-output relationships among the independent modules. (3) The collector network structure was used to create a block-based model of the GFL photovoltaic and GFM energy storage hybrid power generation system. (4) An equivalent grid model that matched the GFL photovoltaic and GFM energy storage hybrid power generation system was then constructed. (5) Interfaces between the GFL photovoltaic and GFM energy storage hybrid power generation system and the grid were established and used to connect the hybrid system to the grid to form a closed-loop system model, as shown in Fig. 3.

In the graphical block-based modeling structure shown in Fig. 3, $\Delta i_{d,L}$ and $\Delta i_{q,L}$ represent the d/q-axis output currents of the GFL photovoltaic grid-side converter; $\Delta U_{dc,L}$ denotes the DC voltage of the GFL photovoltaic system; $\Delta U_{dq,L}$ represents the d/q-axis terminal voltage of the GFL photovoltaic system; $\Delta E_{d,L}$ and $\Delta E_{q,L}$ represent the d/q-axis output voltages of the GFL photovoltaic grid-side converter; $\Delta U_{d,M}$ and $\Delta U_{q,M}$ represent the d/q-axis terminal voltages of the GFM energy storage system; $\Delta i_{sd,M}$ and $\Delta i_{sq,M}$ represent the d/q-axis currents of the GFM energy storage filter inductor; $\Delta E_{d,M}$ and $\Delta E_{q,M}$ represent the d/q-axis output voltages of the GFM energy storage grid-side converter; $\Delta i_{gd,M}$ and $\Delta i_{gq,M}$ represent the d/q-axis output currents of the GFM energy storage grid-side converter; and ΔU_{pccd} and ΔU_{pccq} represent the d/q-axis voltages at the PCC.

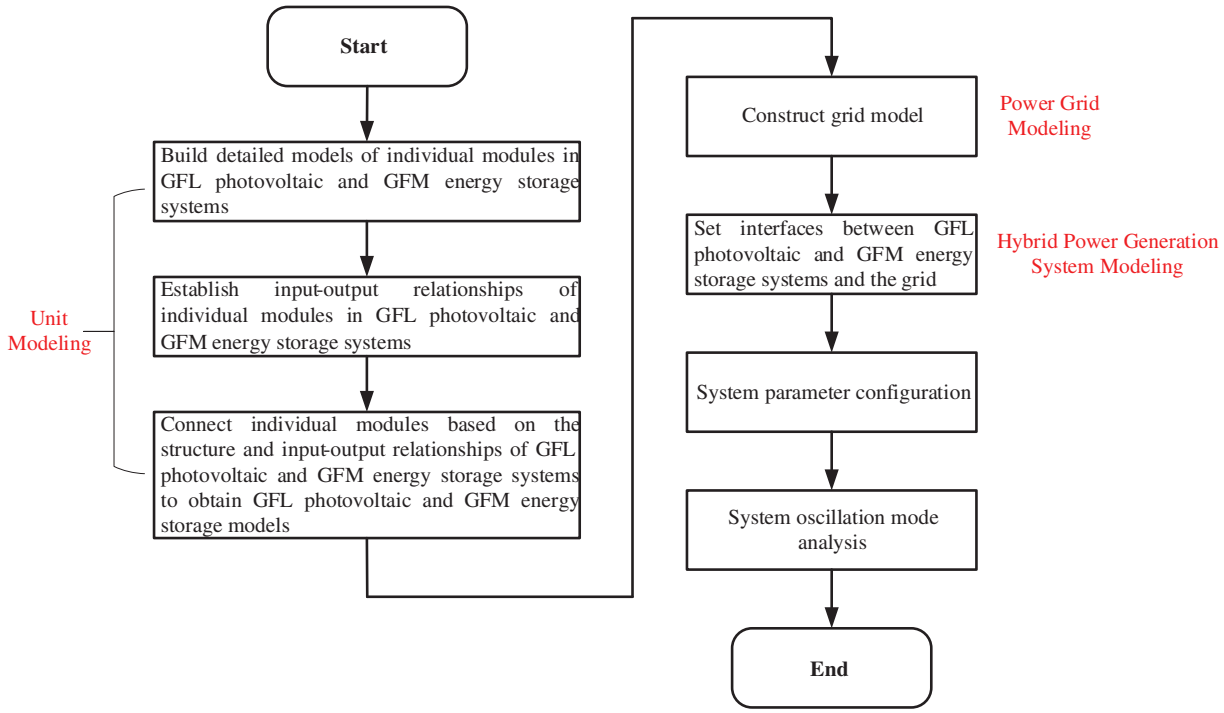


Figure 2: Graphical block-based modeling process

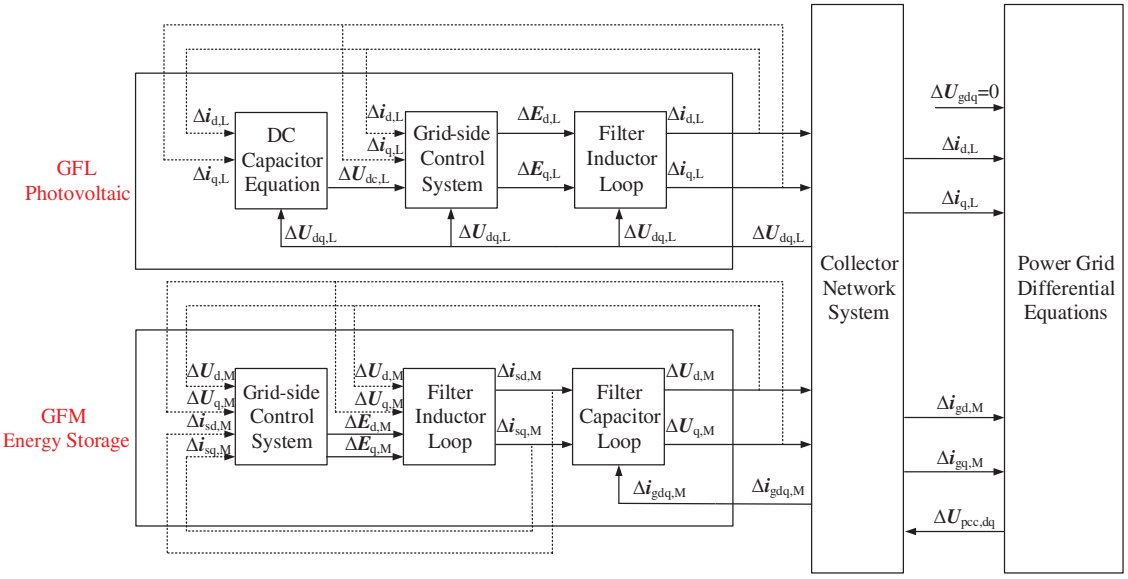


Figure 3: Graphical block-based modeling structure

Traditional linearized models based on derived state-space equations and visual graphical block-based linearized models were built in Matlab/Simulink and an electromagnetic transient simulation model was constructed in PSCAD. The system parameters are provided in the appendix. These were used to validate the effectiveness of the proposed graphical block-based modeling approach. At t = 10 s, an identical power step disturbance was applied (power reduced from 0.3 to 0.23 MW) and active power P_L response curves from

the traditional linearized model, the graphical block-based model, and the time-domain simulation model were obtained, as shown in Fig. 4. The results show that the traditional linearized model and the graphical block-based model for the GFL photovoltaic and GFM energy storage system were in near perfect agreement, which validated the effectiveness of the graphical block-based modeling method. Furthermore, both models aligned closely with the response curve of the time-domain simulation model, which confirmed the validity of the traditional linearized model and the graphical block-based model.

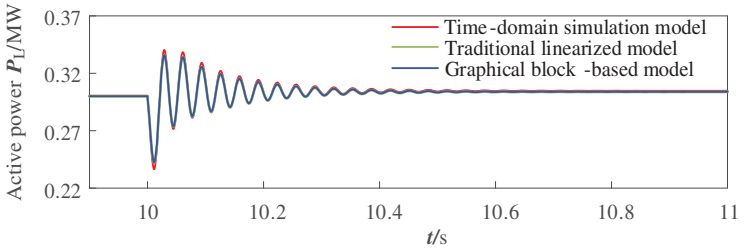


Figure 4: Model validation: active power P_L response curves

The system eigenvalues identified by the graphical block-based model of the GFL photovoltaic and GFM energy storage hybrid power generation system are listed in Table 1. The system eigenvalues comprised of eight oscillation modes: two high-frequency oscillation modes: $\lambda_{11/12}$ (1410.24 Hz) and $\lambda_{13/14}$ (1357.50 Hz); one supersynchronous oscillation mode: $\lambda_{1/2}$ (82.30 Hz); one subsynchronous oscillation mode: $\lambda_{4/5}$ (30.40 Hz); and four low-frequency oscillation modes: $\lambda_{6/7}$ (4.87 Hz), $\lambda_{8/9}$ (2.11 Hz), $\lambda_{19/20}$ (8.01 Hz), and $\lambda_{22/23}$ (1.44 Hz). The dominant subsynchronous oscillation eigenvalue for the GFL photovoltaic and GFM energy storage hybrid power generation system was $\lambda_{4/5}$.

Table 1: Eigenvalues of GFL photovoltaic and GFM energy storage hybrid power generation system

Mode	Eigenvalue	Oscillation frequency/Hz	Damping ratio
$\lambda_{1/2}$	$-302.48 \pm j517.12$	82.30	0.5049
λ_3	-474.78	/	1.0000
$\lambda_{4/5}$	$-6.45 \pm j190.98$	30.40	0.0337
$\lambda_{6/7}$	$-35.29 \pm j30.61$	4.87	0.7554
$\lambda_{8/9}$	$-7.80 \pm j13.26$	2.11	0.5070
λ_{10}	-25.46	/	1.0000
$\lambda_{11/12}$	$-1064.6 \pm j8860.8$	1410.24	0.1193
$\lambda_{13/14}$	$-1117.5 \pm j8529.4$	1357.50	0.1299
λ_{15}	-1893.3	/	1.0000
λ_{16}	-1261.0	/	1.0000
λ_{17}	-948.55	/	1.0000
λ_{18}	-920.92	/	1.0000
$\lambda_{19/20}$	$-241.51 \pm j50.30$	8.01	0.9790
λ_{21}	-35.58	/	1.0000
$\lambda_{22/23}$	$-2.26 \pm j9.06$	1.44	0.2422
λ_{24}	-0.33	/	1.0000
λ_{25}	-50.08	/	1.0000

4 Root Locus Analysis and Simulation Verification

In this section, based on the constructed graphical block-based model, the impact of grid strength, operating conditions, and key control parameters of GFM energy storage on the sub-synchronous oscillation characteristics of the solar-storage hybrid power generation system is systematically analyzed using the root locus method. Furthermore, the underlying mechanisms governing the influence of key GFM energy storage control parameters on system sub-synchronous oscillations are systematically elucidated. A corresponding electromagnetic transient simulation model of the GFL photovoltaic and GFM energy storage hybrid power generation system was built in PSCAD using data from Fig. 1. The parameters of the GFL photovoltaic and GFM energy storage hybrid power generation system are listed in Table 2.

Table 2: System parameters

	Symbol	Parameters	Values/Unit
Main parameters of GFL photovoltaic system	$S_{base,L}$	Rated capacity	0.5/MW
	$C_{dc,L}$	DC-side capacitor	0.09/F
	$u_{dc,L}$	Rated DC-side capacitor voltage	0.7/kV
	$L_{s,L}$	Inverter filter inductor	0.00015/H
	L_1	Collector line inductance	0.000002/H
	G_1/T_1	Filter parameters	1.06/0.0011
	$k_{p1,L}/k_{i1,L}$	PLL proportional/integral coefficients	50/900
	$k_{p2,L}/k_{i2,L}$	Active voltage proportional/integral coefficients	10/303.0303
	$k_{p3,L}/k_{i3,L}$	Active current proportional/integral coefficients	0.026/5
	$k_{p4,L}/k_{i4,L}$	Reactive current proportional/integral coefficients	0.2/5
Main parameters of GFM energy storage system	$S_{base,M}$	Rated capacity	0.15/MW
	$C_{dc,M}$	DC-side capacitor	0.09/F
	$u_{dc,M}$	Rated DC-side capacitor voltage	0.7/kV
	$L_{s,M}$	Inverter filter inductor	0.0001/H
	$C_{s,M}$	Filter capacitor	0.00025/F
	L_2	Collector line inductance	0.0000012/H
	J/D_p	Virtual active inertia/Virtual active damping	0.1/3.56
	τ/D_q	Virtual reactive inertia/Virtual reactive damping	2/100
	G_2/T_2	Filter parameters	1.06/0.0011
	$k_{p1,M}/k_{i1,M}$	Active voltage proportional/integral coefficients	2.7/80
	$k_{p2,M}/k_{i2,M}$	Reactive voltage proportional/integral coefficients	3/80
	$k_{p3,M}/k_{i3,M}$	Active current proportional/integral coefficients	0.3/100

(Continued)

Table 2 (continued)

	Symbol	Parameters	Values/Unit
	$k_{p4,M}/k_{i4,M}$	Reactive current proportional/integral coefficients	0.3/100
Main parameters of power grid	U_g	Grid rated voltage	0.38/kV
	L_g	Line inductance	0.00035/H

4.1 Influence of Operating Condition on Dominant Subsynchronous Oscillation Eigenvalue $\lambda_{4/5}$

When the SCR = 1.6 and with the other parameters held constant, perturbing the GFL photovoltaic output power P_L from 0.1 to 0.5 yields the root locus of the dominant system subsynchronous oscillation eigenvalue $\lambda_{4/5}$, as shown in Fig. 5. As P_L gradually increases, the eigenvalue $\lambda_{4/5}$ gradually shifts toward the right-half plane, indicating reduced system stability. When P_L = 0.45, $\lambda_{4/5}$ becomes 0.17 ± *j*184.58, with a positive real part, signifying that the system loses stability.

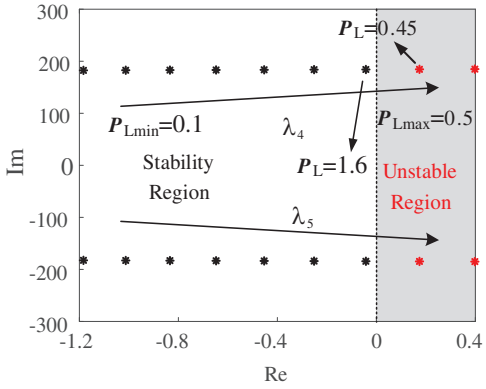


Figure 5: Root locus of $\lambda_{4/5}$ under different operating conditions

The response curves of the system DC voltage $u_{dc,L}$ and output power increment ΔP_L under different operating conditions and when the system SCR decreased from 3.0 to 1.6 at t = 10 s are shown in Fig. 6. The blue curve rep-resents P_L = 0.3 MW, while the red curve represents P_L = 0.45 MW. When P_L = 0.45, the system DC voltage $u_{dc,L}$ and output power increment ΔP_L showed subsynchronous oscillation instability with an oscillation frequency of 27.0 Hz. However, when P_L = 0.3 MW, the system DC voltage $u_{dc,L}$ and output power increment ΔP_L showed damped oscillations and the system was stable. The simulation results were consistent with the theoretical analysis. It can thus be concluded that as the output power of the GFL photovoltaic system increases, the system stability margin decreases accordingly.

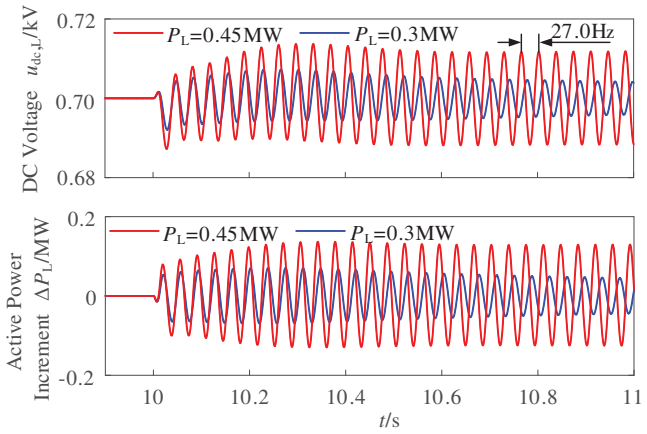


Figure 6: Response curves of $u_{dc,L}$ and ΔP_L under different operating conditions

4.2 Influence of SCR on Dominant Subsynchronous Oscillation Eigenvalue $\lambda_{4/5}$

Decreasing the Short-Circuit Ratio (SCR) from 2.0 to 1.3 and leaving the other parameters the same produced the root locus for the dominant system subsynchronous oscillation eigenvalue $\lambda_{4/5}$, as shown in Fig. 7. As the SCR decreased, $\lambda_{4/5}$ gradually moved toward the right-half plane, which indicated that the system was less stable. When the SCR = 1.5, $\lambda_{4/5}$ was 0.47 ± j182.21 with a positive real part, which meant that the system was not stable.

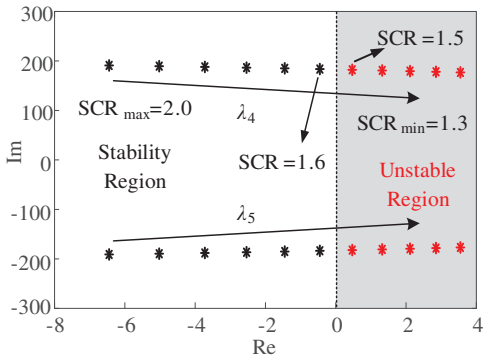


Figure 7: Root locus of $\lambda_{4/5}$ under different SCR conditions

The response curves for the system DC voltage $u_{dc,L}$ and output power P_L at t = 10 s and after the SCR had decreased from 3.0 to 1.6 (blue curve) and 1.5 (red curve) are shown in Fig. 8. When the SCR = 1.5, the system DC voltage $u_{dc,L}$ and output power P_L experienced subsynchronous oscillation instability with an oscillation frequency of 27.1 Hz. When the SCR = 1.6, the system DC voltage $u_{dc,L}$ and output power P_L showed damped oscillations and the system was stable. The simulation results were consistent with the theoretical analysis and system was stable under weak grid conditions.

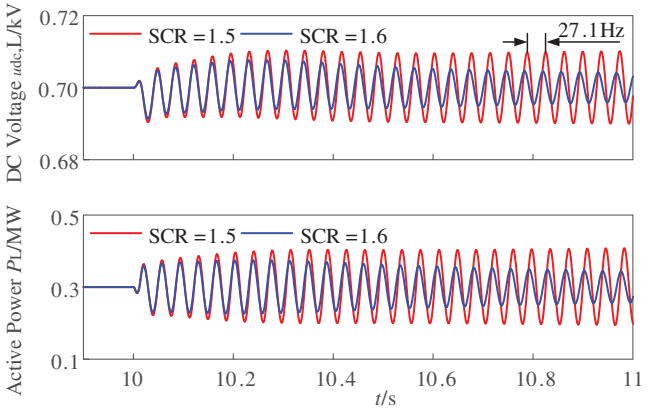


Figure 8: Response curves of $u_{dc,L}$ and P_L under different SCR conditions

4.3 Influence of GFM Energy Storage Active Voltage Proportional Coefficient $k_{p1,M}$ on Dominant Subsynchronous Oscillation Eigenvalue $\lambda_{4/5}$

When the SCR = 1.6 and with the other parameters held constant, decreasing the $k_{p1,M}$ from 4.0 to 2.0 produced the root locus for the dominant system subsynchronous oscillation eigenvalue $\lambda_{4/5}$, as shown in Fig. 9. As $k_{p1,M}$ decreased, $\lambda_{4/5}$ gradually shifted toward the right-half plane, which indicated that the system was less stable. When $k_{p1,M}$ = 2.4, $\lambda_{4/5}$ became 0.43 ± *j*183.81 with a positive real part, which showed that the system was not stable.

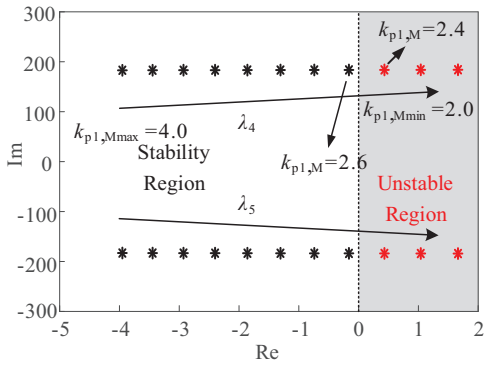


Figure 9: Root locus of $\lambda_{4/5}$ under different $k_{p1,M}$ conditions

The response curves of the system DC voltage $u_{dc,L}$ and output power P_L under different $k_{p1,M}$ values and when the system SCR decreased from 3.0 to 1.6 at t = 10 s are shown in Fig. 10. The blue curve represents $k_{p1,M}$ = 2.7, while the red curve represents $k_{p1,M}$ = 2.4. When $k_{p1,M}$ = 2.4, the system DC voltage $u_{dc,L}$ and output power P_L showed subsynchronous oscillation instability with an oscillation frequency of 27.2 Hz. However, when $k_{p1,M}$ = 2.7, the system DC voltage $u_{dc,L}$ and output power P_L showed damped oscillations and the system was stable. The simulation results were consistent with the theoretical analysis. Therefore, appropriately increasing the grid-forming active voltage proportional coefficient $k_{p1,M}$ can enhance the stability of the hybrid system.

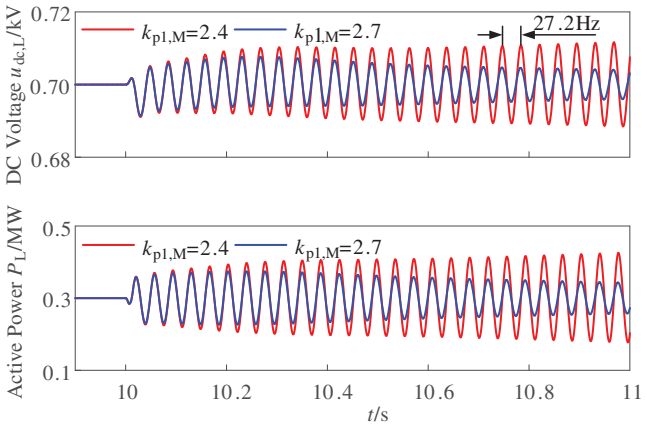


Figure 10: Response curves of $u_{dc,L}$ and P_L under different $k_{p1,M}$ conditions

4.4 Influence of GFM Energy Storage ReactiveVoltage Proportional Coefficient $k_{p2,M}$ on Dominant Subsynchronous Oscillation Eigenvalue $\lambda_{4/5}$

Decreasing $k_{p2,M}$ from 4.2 to 2.2 when the SCR = 1.6 and with the other parameters held constant produced the root locus for the dominant system subsynchronous oscillation eigenvalue $\lambda_{4/5}$, as shown in Fig. 11. As $k_{p2,M}$ decreased, $\lambda_{4/5}$ gradually shifted toward the right-half plane, which indicated that the system was less stable. When $k_{p2,M}$ = 2.8, $\lambda_{4/5}$ became 0.27 ± *j*184.78 with a positive real part, which signifying that the system was unstable.

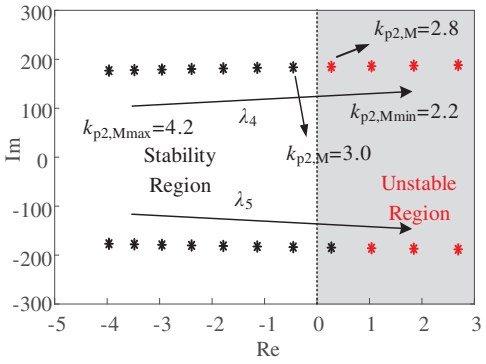


Figure 11: Root locus of $\lambda_{4/5}$ under different $k_{p2,M}$ conditions

The response curves of the system DC voltage $u_{dc,L}$ and output power P_L at different $k_{p2,M}$ values when the system SCR decreased from 3.0 to 1.6 at t = 10 s are shown in Fig. 12. The blue curve represents $k_{p2,M}$ = 3.0, while the red curve represents $k_{p2,M}$ = 2.8. When $k_{p2,M}$ = 2.8, the system DC voltage $u_{dc,L}$ and output power P_L showed subsynchronous oscillation instability with an oscillation frequency of 27.0 Hz. However, when $k_{p2,M}$ = 3.0, the system DC voltage $u_{dc,L}$ and output power P_L showed damped oscillations and the system was stable. The simulation results were consistent with the theoretical analysis. Therefore, appropriately increasing the grid-forming reactive voltage proportional coefficient $k_{p2,M}$ can enhance the stability of the hybrid system.

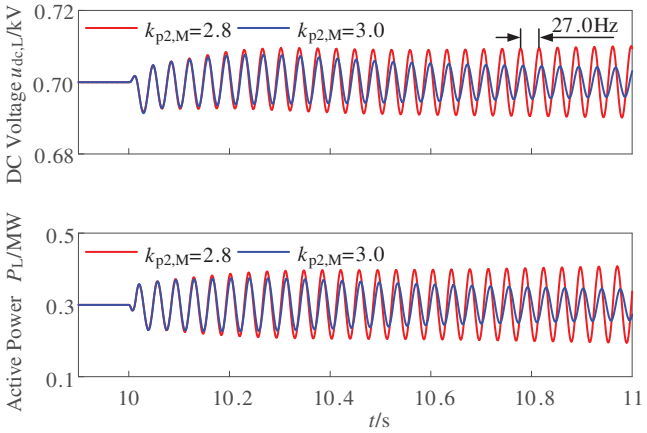


Figure 12: Response curves of $u_{dc,L}$ and P_L under different $k_{p2,M}$ conditions

4.5 Influence of GFM Energy Storage Reactive Voltage Integral Coefficient $k_{i2,M}$ on Dominant Subsynchronous Oscillation Eigenvalue $\lambda_{4/5}$

Decreasing $k_{i2,M}$ from 165 to 15 when the SCR = 1.6 and the other parameters were held constant produced the root locus for the dominant system subsynchronous oscillation eigenvalue $\lambda_{4/5}$, as shown in Fig. 13. As $k_{i2,M}$ decreased, $\lambda_{4/5}$ gradually shifted toward the right-half plane, which indicated that the system was less stable. When $k_{i2,M}$ = 60, $\lambda_{4/5}$ was 0.17 ± j183.25 with a positive real part, which meant that the system was not stable.

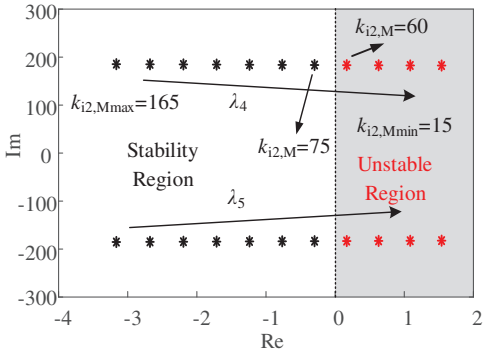


Figure 13: Root locus of $\lambda_{4/5}$ under different $k_{i2,M}$ conditions

The response curves for the system DC voltage $u_{dc,L}$ and output power P_L under different $k_{i2,M}$ values when the system SCR was reduced from 3.0 to 1.6 at t = 10 s are shown in Fig. 14. The blue curve represents $k_{i2,M}$ = 80, while the red curve represents $k_{i2,M}$ = 60. When $k_{i2,M}$ = 60, the system DC voltage $u_{dc,L}$ and output power P_L showed subsynchronous oscillation instability with an oscillation frequency of 27.2 Hz. However, when $k_{i2,M}$ = 80, the system DC voltage $u_{dc,L}$ and output power P_L showed damped oscillations and the system was stable The simulation results were consistent with the theoretical analysis. Therefore, appropriately increasing the grid-forming reactive voltage integral coefficient $k_{i2,M}$ can enhance the stability of hybrid system.

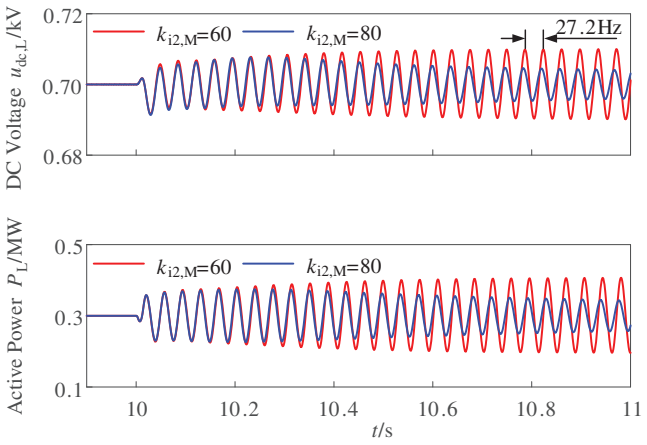


Figure 14: Response curves of $u_{dc,L}$ and P_L under different $k_{i2,M}$ conditions

4.6 Influence of GFM Energy Storage Reactive Current Integral Coefficient $k_{i4,M}$ on Dominant Subsynchronous Oscillation Eigenvalue $\lambda_{4/5}$

Decreasing $k_{i4,M}$ from 160 to 60 when the SCR = 1.6 and the other parameters were held constant produced the root locus of the dominant system subsynchronous oscillation eigenvalue $\lambda_{4/5}$, as shown in Fig. 15. As $k_{i4,M}$ decreased, $\lambda_{4/5}$ gradually shifted toward the right-half plane, which indicated that the system was less stable. When $k_{i4,M}$ = 70, $\lambda_{4/5}$ was 0.09 ± j183.78 with a positive real part, which meant that the system was not stable.

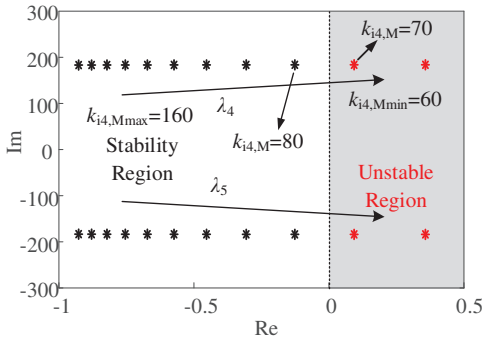


Figure 15: Root locus of $\lambda_{4/5}$ under different $k_{i4,M}$ conditions

The response curves of the system DC voltage $u_{dc,L}$ and output power P_L under different $k_{i4,M}$ values when the system SCR decreased from 3.0 to 1.6 at t = 10 s are shown in Fig. 16. The blue curve represents $k_{i4,M}$ = 100, while the red curve represents $k_{i4,M}$ = 70. When $k_{i4,M}$ = 70, the system DC voltage $u_{dc,L}$ and output power P_L showed subsynchronous oscillation instability with an oscillation frequency of 26.9 Hz. However, when $k_{i4,M}$ = 100, the system DC voltage $u_{dc,L}$ and output power P_L showed damped oscillations and the system was stable. The simulation results were consistent with the theoretical analysis. Therefore, appropriately increasing the grid-forming reactive current integral coefficient $k_{i4,M}$ can enhance the stability of the hybrid system.

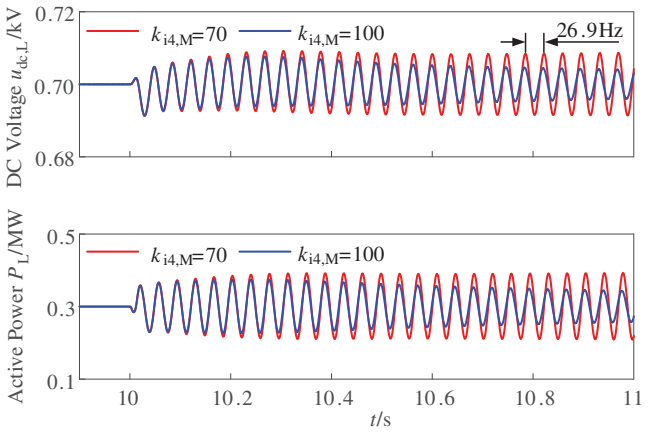


Figure 16: Response curves of $u_{dc,L}$ and P_L under different $k_{i4,M}$ conditions

4.7 Impact of Multi-Parameter Coupling Characteristics on Dominant Subsynchronous Oscillation Eigenvalue $\lambda_{4/5}$

Under the conditions of SCR = 1.6 and GFL photovoltaic output power P_L = 0.3 MW, this paper qualitatively analyzes the influence of the coupling characteristics between active voltage proportional coefficient $k_{p1,M}$ and the reactive voltage proportional coefficient $k_{p2,M}$ on the real part of the dominant system subsynchronous oscillation eigenvalue, based on the eigenvalue criterion. The results are shown in Fig. 17. Fig. 17 illustrates the distribution characteristics of the real part of the dominant subsynchronous oscillation eigenvalue as $k_{p1,M}$ and $k_{p2,M}$ vary. The study reveals that as $k_{p1,M}$ or $k_{p2,M}$ increases, the real part of the dominant eigenvalue decreases accordingly; conversely, a decrease in either parameter leads to an increase in this real part. Notably, when $k_{p1,M}$ or $k_{p2,M}$ is set too small, the real part of the dominant eigenvalue becomes positive, causing the system to become unstable. Furthermore, when $k_{p1,M}$ is set to a larger value, $k_{p2,M}$ can maintain system stability within a relatively wide range. This conclusion provides an important theoretical basis for optimizing controller parameters in solar-storage hybrid power generation systems, indicating that appropriately increasing both $k_{p1,M}$ and $k_{p2,M}$ helps enhance system stability margins.

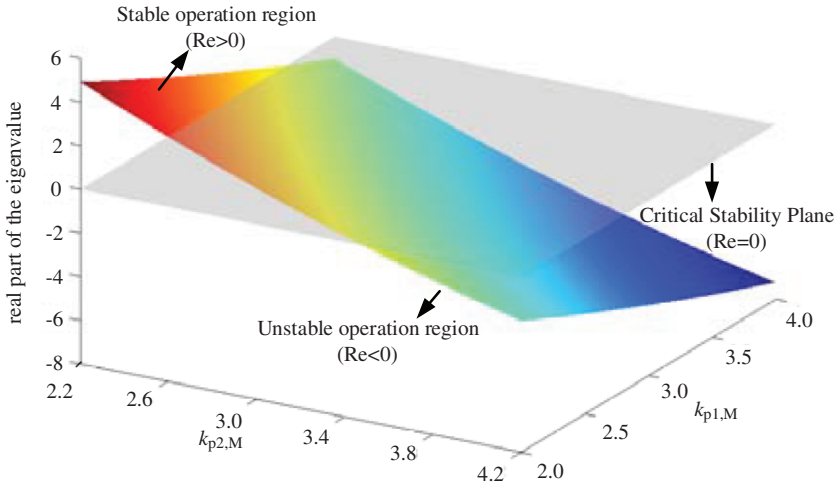


Figure 17: Influence of $k_{p1,M}$ and $k_{p2,M}$ variations on the real part of the dominant system eigenvalue

Under the conditions of SCR = 1.6 and GFL photovoltaic output power P_L = 0.3 MW, this paper qualitatively analyzes the influence of the coupling characteristics between the reactive voltage proportional coefficient $k_{p2,M}$ and the integral coefficient $k_{i2,M}$ on the real part of the dominant system subsynchronous oscillation eigenvalue, based on eigenvalue criteria. The results are shown in Fig. 18. Fig. 18 illustrates the distribution characteristics of the real part of the dominant subsynchronous oscillation eigenvalue as $k_{p2,M}$ and $k_{i2,M}$ vary. The study reveals that as either $k_{p2,M}$ or $k_{i2,M}$ increases, the real part of the dominant eigenvalue decreases accordingly; conversely, a decrease in either parameter leads to an increase in this real part. Notably, when $k_{p2,M}$ or $k_{i2,M}$ is set too small, the real part of the dominant eigenvalue becomes positive, causing the system to become unstable. Furthermore, when $k_{p2,M}$ is set to a relatively large value, $k_{i2,M}$ can maintain system stability across a broader range. This conclusion provides an important theoretical basis for optimizing controller parameters in solar-storage hybrid power generation systems, indicating that appropriately increasing both $k_{p2,M}$ and $k_{i2,M}$ helps enhance system stability margins.

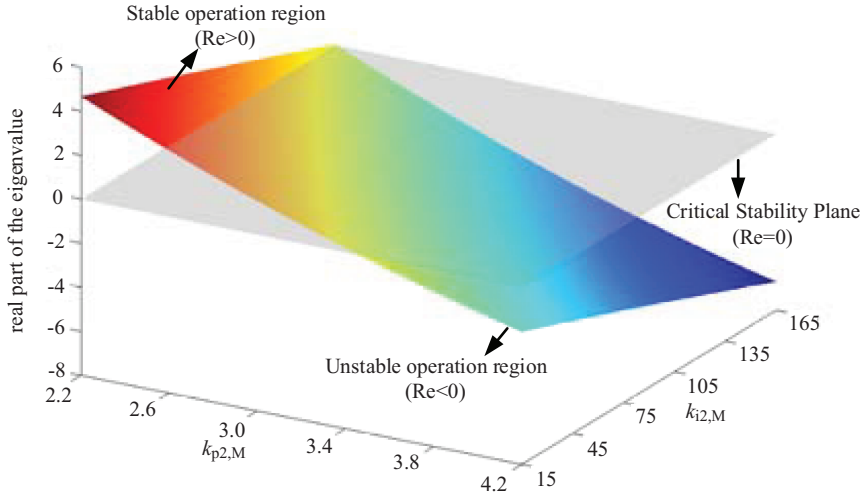


Figure 18: Influence of $k_{p2,M}$ and $k_{i2,M}$ variations on the real part of the dominant system eigenvalue

Under the conditions of SCR = 1.6 and GFL photovoltaic output power P_L = 0.3 MW, this paper qualitatively analyzes the influence of the coupling characteristics between the reactive voltage integral coefficient $k_{i2,M}$ and the reactive current integral coefficient $k_{i4,M}$ on the real part of the dominant system subsynchronous oscillation eigenvalue, based on the eigenvalue criterion. The results are shown in Fig. 19. Fig. 19 illustrates the distribution characteristics of the real part of the dominant subsynchronous oscillation eigenvalue as $k_{i2,M}$ and $k_{i4,M}$ vary. The study reveals that as $k_{i2,M}$ or $k_{i4,M}$ increases, the real part of the dominant eigenvalue decreases accordingly; conversely, a decrease in either parameter leads to an increase in this real part. Notably, when $k_{i2,M}$ or $k_{i4,M}$ is set too small, the real part of the dominant eigenvalue becomes positive, causing the system to become unstable. Furthermore, when $k_{i2,M}$ is set to a larger value, $k_{i4,M}$ can maintain system stability within a relatively wide range. This conclusion provides an important theoretical basis for optimizing controller parameters in solar-storage hybrid power generation systems, indicating that appropriately increasing both $k_{i2,M}$ and $k_{i4,M}$ helps enhance system stability margins.

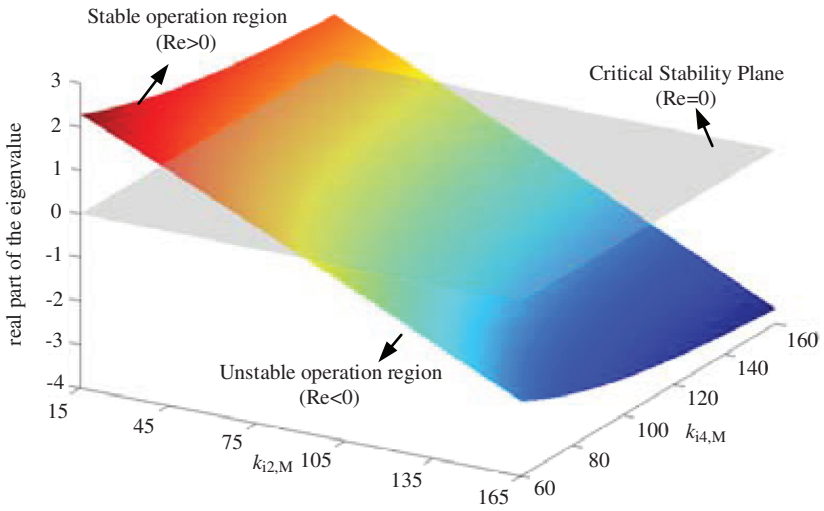


Figure 19: Influence of $k_{i2,M}$ and $k_{i4,M}$ variations on the real part of the dominant system eigenvalue

4.8 Advantages Over the Existing Solutions

To accurately address the modeling challenges constraining the small-signal stability analysis of hybrid solar-storage power generation systems, this paper systematically summarizes the characteristics and limitations of existing models through a comprehensive review of mainstream research literature, as detailed in Table 3. Frequency-domain impedance models and state-space models are two typical approaches for studying the small-signal stability of such systems. Frequency-domain impedance models divide the system into equipment subsystems and grid subsystems, establish equivalent impedance models for each, and apply the Nyquist criterion for stability assessment. While the constructed models exhibit strong scalability, their inherent "port-based" and "black-box" characteristics make it difficult to directly observe the dynamic processes of internal state variables. Additionally, in complex systems involving multiple converters, accurately identifying dominant instability paths remains challenging, limiting their in-depth application in engineering practice. State-space models evaluate system stability by solving model eigenvalues, offering advantages in theoretical rigor and result accuracy. However, they suffer from high computational complexity, difficult solution processes, and poor scalability, particularly when applied to large-scale complex systems.

Table 3: Model comparison

Analysis and Research	Advantages	Disadvantages	Ref.
Frequency-domain impedance model	1. Simple model structure 2. Intuitive derivation process	1. Poor visibility 2. Complex for multi-machine system analysis; interaction paths are difficult to identify	[11–13]
Traditional state-space model	1. Provides comprehensive modal characteristic information 2. High accuracy of results 3. Wide applicability	1. Poor scalability 2. High computational complexity	[14–16]

(Continued)

Table 3 (continued)

Analysis and Research	Advantages	Disadvantages	Ref.
Model proposed in this paper (Graphical Block-Based Model)	1. Automatically generates system equations with high modeling effi ciency 2. Provides complete modal characteristics and high-accuracy results 3. Exhibits strong scalability and supports multi-machine systems 4. Demonstrates outstanding visual modeling and analysis capabilities 5. Applicable to various complex stability analysis scenarios	1. Requires the division of modules and the definition of their respective interfaces 2. Depends on specific simulation platforms	/

To overcome the limitations of existing methods, this paper proposes a graphical block-based modeling approach that abstracts system components into graphical modules with well-defined input-output interfaces. By visually constructing the model in the Matlab/Simulink environment and leveraging its built-in functions to automatically generate global system equations, this method fundamentally avoids algebraic errors that are difficult to eliminate in traditional manual derivations and eliminates the need for cumbersome intermediate variable elimination processes. Compared to impedance models, this method offers greater visibility. In contrast to traditional state-space models, it significantly improves modeling efficiency and scalability while maintaining model accuracy. Based on the established graphical block-based model, this study further identifies the key eigenvalues dominating the subsynchronous oscillations in the hybrid system composed of GFL photovoltaic and GFM energy storage units. Using root locus analysis, it elucidates the dynamic influence patterns of GFM energy storage control parameters on the small-signal stability of the system. The results indicate that appropriately increasing the active voltage proportional coefficient $k_{p1,M}$, the reactive voltage proportional coefficient $k_{p2,M}$, the reactive voltage integral coefficient $k_{i2,M}$, and the reactive current integral coefficient $k_{i4,M}$ of the GFM energy storage can effectively enhance the small-signal stability of the system. This research provides a theoretical foundation for the adaptive tuning of control parameters in hybrid solar-storage systems under different operating conditions.

4.9 Engineering Challenges and Technical Prospects

The graphical block-based modeling method provides an innovative solution for analyzing the small-signal stability of hybrid solar-storage power generation systems. The core of this method lies in abstracting physical components such as photovoltaic arrays, energy storage converters, and phase-locked loops into graphical modules with standardized interfaces. System assembly is achieved through visual drag-and-drop operations on the Matlab/Simulink platform, and full-order state-space equations are automatically generated using built-in linearization tools. This modeling paradigm fundamentally avoids algebraic errors and the complexity of eliminating intermediate variables, which are difficult to prevent in traditional manual derivations. Simultaneously, it preserves the physical transparency of the system, enabling researchers to intuitively track the dynamic evolution of internal state variables, thereby realizing "white-box" modeling and analysis.

In practical engineering applications, this method demonstrates multidimensional value: during the grid planning phase, it allows for rapid assessment of the impact of newly grid-connected equipment on regional stability; after oscillation incidents, it enables precise reconstruction of instability mechanisms; in

multi-converter power stations, it provides a visual platform for the collaborative optimization of controller parameters; in research and teaching, it serves as an effective instructional tool for understanding the stability mechanisms of power-electronized grids. The balance between modeling efficiency and physical intuitiveness makes it particularly suitable for scenarios requiring rapid iteration and mechanistic exploration.

However, the engineering promotion of this method faces a series of challenges: model accuracy heavily depends on the accuracy of the foundational modules, with a significant "garbage in, garbage out" risk; large-scale systems still encounter the "curse of dimensionality" in eigenvalue computation; it imposes high demands on users' professional theoretical knowledge; and its implementation is deeply reliant on commercial software ecosystems, and integration with existing simulation platforms in power enterprises poses obstacles. As a small-signal linearization method, its inherent limitations include the inability to simulate large-disturbance processes such as fault transients and difficulty in accurately representing control strategies with complex logic switching.

In summary, graphical block-based modeling serves as an effective bridge connecting physical objects and mathematical analysis. It is a "specialized surgical tool" for refined stability diagnosis rather than a "universal key" for full-system simulation. Future research should focus on developing modular standard libraries, advancing reduced-order computation methods, establishing validation processes with measured data, and promoting the construction of open-source toolchains to better support the stable operation of power systems with high penetration of renewable energy.

5 Conclusion

The small-signal stability of a GFL photovoltaic and GFM energy storage hybrid power generation system was investigated by constructing a full-order linearized state-space model of the system based on graphical block-based modeling. This proposed new method avoids the potential human calculation errors associated with traditional state-space equation derivation and eliminates the need for intermediate algebraic operations to remove intermediate variables. This alternative approach significantly improved modeling efficiency. The accuracy of the graphical block-based modeling method was verified by comparing the traditional linearized model with the graphical block-based linearized model. The proposed graphical block model was used to identify the dominant subsynchronous oscillation eigenvalues for the GFL photovoltaic and GFM energy storage hybrid power generation system. In addition, the dynamic influence of the GFM energy storage control parameters on the small-signal stability of the system was analyzed using a root locus analysis. The following conclusions can be drawn after the results had been validated using simulations:

(1) The GFL photovoltaic and GFM energy storage hybrid power generation system has a certain degree of operational capability under weak grid conditions.
(2) The proposed graphical block-based modeling method eliminates the potential human calculation errors associated with traditional state-space equation derivation and significantly improves modeling efficiency by avoiding the intermediate algebraic operations required to eliminate the intermediate variables.
(3) Appropriately increasing the GFM energy storage parameters—specifically, the active voltage proportional coefficient $k_{p1,M}$, the reactive voltage proportional coefficient $k_{p2,M}$, the reactive voltage integral coefficient $k_{i2,M}$, and the reactive current integral coefficient $k_{i4,M}$—can effectively enhance the small-signal stability of hybrid power generation system.

These results provide a theoretical foundation for subsequently improving the small-signal stability of solar-storage hybrid systems through optimized tuning of the GFM energy storage control parameters.

Acknowledgement: Not applicable.

Funding Statement: This research was funded by Supported by the Science and Technology Project of State Grid Corporation of China (2025220202000070).

Author Contributions: The authors confirm contribution to the paper as follows: Conceptualization—ideas, formulation or evolution of overarching research goals and aims, Qiang Liu and Yongqiang Zhou; writing—original draft—preparation, creation and/or presentation of the published work, specifically writing the initial draft (including substantive translation), Chaoyang Lu; writing—review & editing—preparation, creation and/or presentation of the published work by those from the original research group, specifically critical review, commentary or revision—including pre- or post-publication stages, Zhen Yan; project administration—management and coordination responsibility for the research activity planning and execution, Gangui Yan and Yanwen Li; software and validation—oversight and leadership responsibility for the research activity planning and execution, including mentorship external to the core team and verification, whether as a part of the activity or separate, of the overall replication/reproducibility of results/experiments and other research outputs, Yupeng Wang. All authors reviewed the results and approved the final version of the manuscript.

Availability of Data and Materials: Not applicable.

Ethics Approval: Not applicable.

Conflicts of Interest: The authors declare no conflicts of interest to report regarding the present study.

Abbreviations

GFL	Grid-Following
GFM	Grid-Forming
PCC	Point of Common Coupling
SCR	Short-Circuit Ratio

References

1. Leite R, Oleskkovicz M. The joint application of photovoltaic generation and distributed or concentrated energy storage systems in a low voltage distribution network: a case study. IEEE Lat Am Trans. 2023;21(10):1122–31. doi:10.1109/TLA.2023.10255443.
2. Kittner N, Lill F, Kammen DM. Energy storage deployment and innovation for the clean energy transition. Nat Energy. 2017;2(9):17125. doi:10.1038/nenergy.2017.125.
3. Zhao F, Xiao C, Chen X, Wang Y. Research on virtual DC generator-based control strategy of DC microgrid with photovoltaic and energy storage. Energy Eng. 2023;120(6):1353–70. doi:10.32604/ee.2023.025976.
4. Lee DJ, Wang L. Small-signal stability analysis of an autonomous hybrid renewable energy power generation/energy storage system part I: time-domain simulations. IEEE Trans Energy Convers. 2008;23(1):311–20. doi:10.1109/TEC.2007.914309.
5. Du B, Zhu J, Hu J, Guo Z, Li Y, Guo J. Electromagnetic oscillation stabilizer for large-scale power electronics-dominated power systems in LTP framework—part I: functional derivative-based measures of modal controllability and observability. IEEE Trans Power Electron. 2025;40(11):17172–85. doi:10.1109/TPEL.2025.3588571.
6. Zhu Y, Wen H, Bu Q, Chu G, Shi H. Flexible power point tracking for photovoltaic systems under partial shading conditions. In: Proceedings of the 2022 IEEE Energy Conversion Congress and Exposition (ECCE); 2022 Oct 9–13; Detroit, MI, USA. p. 1–7. doi:10.1109/ECCE50734.2022.9947430.
7. Chauhan PJ, Dastagiri Reddy B, Panda SK. Seamless transitions of distributed generators in standalone microgrid for unintterupted power supply. In: Proceedings of the 2017 IEEE 18th Workshop on Control and Modeling for Power Electronics (COMPEL); 2017 Jul 9–12; Stanford, CA, USA. p. 1–6. doi:10.1109/compel.2017.8013372.
8. Zhao C, Chai W, Rui B, Chen L. Analysis of sub-synchronous oscillation of virtual synchronous generator and research on suppression strategy in weak grid. Energy Eng. 2023;120(11):2683–705. doi:10.32604/ee.2023.029620.

9. Li M, Zhang X, Fu X, Geng H, Zhao W. Stability studies on PV grid-connected inverters under weak grid: a review. Chin J Electr Eng. 2024;10(4):1–19. doi:10.23919/CJEE.2024.000081.
10. Zhu Q, Guo D, Ruan R, Chai Z, Wang C, Guan Z. The emergency control method for multi-scenario sub-synchronous oscillation in wind power grid integration systems based on transfer learning. Energy Eng. 2025;122(8):3133–54. doi:10.32604/ee.2025.063165.
11. Zhang K, Shi M, Chen X, Shao D, Xu Y, Chen Y. Interaction modeling and stability analysis of grid-forming energy storage system based on SISO transfer functions. IEEE Trans Sustain Energy. 2025;16(1):573–87. doi:10.1109/TSTE.2024.3471801.
12. Dong W, Diao H, Xu J, Kang J, Lv Z. Analysis and parameters design of grid-forming converter for enhancing the stability of photovoltaic storage system under weak grid. IEEE Access. 2024;12(3):134273–84. doi:10.1109/ACCESS.2024.3449340.
13. Magableh MAK, Radwan AAA, Abdel-Rady I, Mohamed Y. Dynamic analysis and stability enhancement of a weak grid-tied hybrid system integrating PV, full-scale wind turbine, and battery storage. IEEE Open J Ind Appl. 2025;6(3):325–49. doi:10.1109/OJIA.2025.3569306.
14. Fang Z, Huang Y, Yan W, Wang D, Tang J, Xie C, et al. Impact analysis of grid-forming and grid-following converter interaction on small-signal stability of parallel systems. Electr Power Autom Equip. 2025;45(02):134–42. (In Chinese). doi:10.16081/j.epae.202410003.
15. Zhao F, Wang X, Zhou Z, Harnefors L, Svensson JR, Kocewiak Ł.H, et al. Control interaction modeling and analysis of grid-forming battery energy storage system for offshore wind power plant. IEEE Trans Power Syst. 2022;37(1):497–507. doi:10.1109/TPWRS.2021.3096850.
16. Magableh MAK, Radwan AAA, Mohamed YAI, El-Saadany EF. A novel reduced-order modeling approach of a grid-tied hybrid photovoltaic–wind turbine–battery energy storage system for dynamic stability analysis. IEEE Open J Power Electron. 2024;5:1459–83. doi:10.1109/OJPEL.2024.3455933.